

ARTICLE

Received 4 Apr 2016 | Accepted 22 Jun 2016 | Published 9 Aug 2016

DOI: 10.1038/ncomms12324

OPEN

# A nickel iron diselenide-derived efficient oxygen-evolution catalyst

Xiang Xu<sup>1,\*</sup>, Fang Song<sup>1,\*</sup> & Xile Hu<sup>1</sup>

Efficient oxygen-evolution reaction catalysts are required for the cost-effective generation of solar fuels. Metal selenides have been reported as promising oxygen-evolution catalysts; however, their active forms are yet to be elucidated. Here we show that a representative selenide catalyst, nickel selenide, is entirely converted into nickel hydroxide under oxygen-evolution conditions. This result indicates that metal selenides are unstable during oxygen evolution, and the *in situ* generated metal oxides are responsible for their activity. This knowledge inspired us to synthesize nanostructured nickel iron diselenide, a hitherto unknown metal selenide, and to use it as a templating precursor to a highly active nickel iron oxide catalyst. This selenide-derived oxide catalyses oxygen evolution with an overpotential of only 195 mV for 10 mA cm<sup>-2</sup>. Our work underscores the importance of identifying the active species of oxygen-evolution catalysts, and demonstrates how such knowledge can be applied to develop better catalysts.

<sup>1</sup>Laboratory of Inorganic Synthesis and Catalysis, Institute of Chemical Sciences and Engineering, Ecole Polytechnique Fédérale de Lausanne (EPFL), EPFL-ISIC-LSCI, BCH 3305, Lausanne CH 1015, Switzerland. \* These authors contributed equally to this work. Correspondence and requests for materials should be addressed to F.S. (email: sofa0318@gmail.com) or to X.H. (email: xile.hu@epfl.ch)

Sunlight-driven water splitting or carbon dioxide ( $\text{CO}_2$ ) reduction to make solar fuels is a promising solution to solar energy storage<sup>1</sup>. Essential to the water splitting and  $\text{CO}_2$  reduction reactions is the oxygen-evolution reaction (OER). This reaction is kinetically sluggish and demands an efficient electrocatalyst<sup>2</sup>. Although noble metal-based catalysts such as  $\text{IrO}_2$  and  $\text{RuO}_2$  exhibit good OER activity, their scarcity and high cost pose great constraints for large-scale applications. Tremendous efforts have been made in recent years to develop non-precious OER catalysts<sup>3,4</sup>. Despite the progress, a significant overpotential is still required for state-of-the-art catalysts. To reach  $10 \text{ mA cm}^{-2}$ , a widely used figure of merit equivalent to  $\sim 12\%$  solar to hydrogen efficiency, nearly all non-precious catalysts need an overpotential of more than 250 mV.

The majority of non-precious OER catalysts are metal oxides and (oxy)hydroxides<sup>3,4</sup>. Recently, a few non-oxide-based OER catalysts including metal phosphides, sulfides and selenides are reported<sup>5–11</sup>. Given the limited stability of these compounds under highly oxidative potentials in alkaline solutions, questions have arisen on the nature of the true active species. Indeed, we and others showed that the surfaces of  $\text{Ni}_2\text{P}$  and  $\text{CoP}$  were transformed into metal oxides during catalysis, which were responsible for the catalytic activity<sup>5–7</sup>. For Ni, Co and Fe sulfides, Chen *et al.* showed that they were entirely transformed into the corresponding metal oxides during OER<sup>8</sup>. Since metal selenides have similar chemical reactivity to metal sulfides, we were surprised by previous reports which suggested stability of bulk  $\text{NiSe}$ ,  $\text{Ni}_3\text{Se}_2$  and  $\text{CoSe}_2$  materials under OER<sup>9–11</sup>. Using a post-catalytic analysis, we show here that  $\text{NiSe}$  is completely converted into nickel hydroxides during OER, indicating that metal oxides or hydroxides are the active and final forms of metal selenides pre-catalysts in OER. This knowledge promoted us to purposely use metal selenides as templating precursors to highly active metal oxide OER catalysts, because methods to produce ultrasmall nanostructured metal

selenides are readily available<sup>12–15</sup>. Following this strategy, we synthesize a hitherto unknown selenide, nickel iron diselenide ( $\text{Ni}_x\text{Fe}_{1-x}\text{Se}_2$ ), which upon *in situ* transformation into oxides, catalyses OER with an overpotential of only 195 mV for a current density of  $10 \text{ mA cm}^{-2}$ . This is until now the most active single-phase OER catalyst in alkaline solutions. The high activity of this  $\text{Ni}_x\text{Fe}_{1-x}\text{Se}_2$ -derived catalyst is largely due to its desirable nanostructure, inherited from its selenide precursor.

## Results

**Active form of  $\text{NiSe}$  in OER.**  $\text{NiSe}$  was synthesized via a hydrothermal approach using Ni foam as the precursor<sup>9</sup>. The electrocatalytic activity of  $\text{NiSe}$  towards OER was investigated in 1 M KOH using a three-electrode electrochemical system. Galvanostatic scan at the current density of  $10 \text{ mA cm}^{-2}$  was used to activate the catalyst. The activity was then measured by linear sweep voltammetry (LSV) at a scan rate of  $1 \text{ mV s}^{-1}$ . The overpotentials to reach  $10 \text{ mA cm}^{-2}$  was  $\sim 253 \text{ mV}$  (Supplementary Fig. 1), in agreement with previous reports. The morphology and composition of the catalyst after catalysis for 12 h were then examined. Transmission electron microscopy (TEM) image showed that single-crystal nanowires of  $\text{NiSe}$  were converted to polycrystalline particles made of ultrathin nanosheets (Fig. 1a,b). Selected area electron diffraction (SAED) pattern of the sample after OER can be indexed to (111), (103) and (301) planes of  $\alpha\text{-Ni}(\text{OH})_2$  (Fig. 1b) (space group:  $P\bar{3}1m$ , JCPDS No. 22-0444). The different lattice fringes in high-resolution TEM (HRTEM) images of samples before and after OER confirmed the total conversion of  $\text{NiSe}$  into  $\text{Ni}(\text{OH})_2$ . Similarly, the elemental mapping of the sample after OER showed that the Se content decreased from 50.2% to 4.0%, but the oxygen content increased from 2.4 to 52.8% during the transformation (Fig. 1c,d). Thus, Se was nearly completely removed while oxygen was incorporated during OER. The above data indicate that  $\text{NiSe}$  is entirely converted into

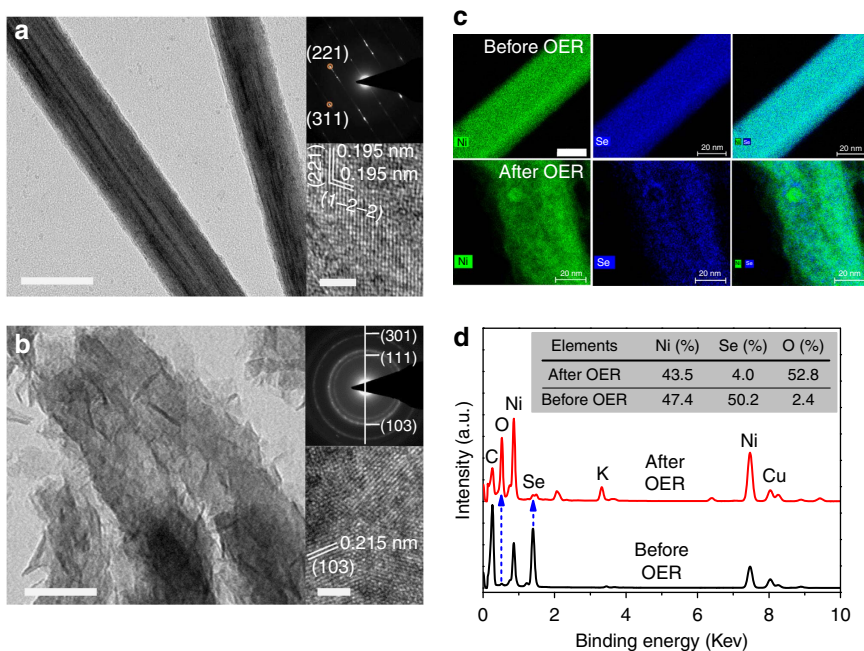


**Figure 1 | Structural and compositional characterization of  $\text{NiSe}$ .** (a,b) TEM and HRTEM images and SAED patterns before (a) and after (b) OER. (c,d) Elemental mapping images and corresponding EDS before and after OER. Colours in elemental mapping images: green for Ni; and blue for Se. Cu and C signals in the EDS are from the copper grid and carbon film that are used to support the sample for TEM measurements. K is due to the residual electrolyte (1 M KOH). The inset in the spectra shows the elemental atomic percentages. Scale bar: (a) 50 nm; and (b) 50 nm. Insets in a,b, 2 nm; and c, 20 nm. EDS, energy-dispersive spectroscopy.

Ni(OH)<sub>2</sub> under OER conditions, which is the active form of the catalyst. Interestingly, the activity of the NiSe-derived Ni(OH)<sub>2</sub> is higher than the most active Ni(OH)<sub>2</sub> nanoparticles prepared by direct synthesis, which requires 300 mV to reach 10 mA cm<sup>-2</sup> (refs 16,17). This result suggests that metal selenides may serve as templating precursors to metal oxides or hydroxides with superior OER activity than those prepared by other methods. With this in mind, we turn our attention to nickel iron selenides, as NiFeO<sub>x</sub> is one of the most active OER catalysts<sup>18–21</sup>.

**Fabrication of Ni<sub>x</sub>Fe<sub>1-x</sub>Se<sub>2</sub>.** Metal selenides normally exist in two forms, mono-selenide (MSe) and diselenides (MSe<sub>2</sub>). We attempted to synthesize both Ni<sub>x</sub>Fe<sub>1-x</sub>Se and Ni<sub>x</sub>Fe<sub>1-x</sub>Se<sub>2</sub>. However, only diselenide Ni<sub>x</sub>Fe<sub>1-x</sub>Se<sub>2</sub> could be obtained. NiSe<sub>2</sub> and FeSe<sub>2</sub> are well-known substances, while Ni<sub>x</sub>Fe<sub>1-x</sub>Se<sub>2</sub> is a hitherto unknown selenide, probably due to a mismatch between the crystal structures of NiSe<sub>2</sub> and FeSe<sub>2</sub>. Both have a cubic structure (space group: Pa-3), but NiSe<sub>2</sub> has a cell parameter of

$a = 5.960 \text{ \AA}$ , while FeSe<sub>2</sub> has a parameter of  $a = 5.776 \text{ \AA}$ . To circumvent this mismatch, a reductive solvothermal process was applied using NiFe-layered double hydroxide (LDH) grown on Ni foam as the precursor. We hypothesized that Ni and Fe were already well dispersed in the crystal lattices of NiFe LDH, so that its selenization might lead to pure-phase Ni<sub>x</sub>Fe<sub>1-x</sub>Se<sub>2</sub> without phase separation between NiSe<sub>2</sub> and FeSe<sub>2</sub>. This approach indeed worked.

Powder X-ray diffraction (PXRD) pattern (Fig. 2a) of the as-synthesized Ni<sub>x</sub>Fe<sub>1-x</sub>Se<sub>2</sub> ( $x = 0.8$ ) indicated the formation of a cubic pyrite-phase metal selenide, similar to NiSe<sub>2</sub> (space group: Pa-3, JCPDS No. 88-1711). The unit cell of cubic metal diselenides is shown in the inset in Fig. 2a. No crystalline impurity was detected. The diffraction peaks of Ni<sub>x</sub>Fe<sub>1-x</sub>Se<sub>2</sub> were shifted to higher angles compared with their counter parts in NiSe<sub>2</sub> (upper right inset in Fig. 2a). The crystal parameter of Ni<sub>x</sub>Fe<sub>1-x</sub>Se<sub>2</sub> is  $a = 5.884 \text{ \AA}$ , which is between NiSe<sub>2</sub> ( $a = 5.960 \text{ \AA}$ ) and FeSe<sub>2</sub> ( $5.776 \text{ \AA}$ ). Ni<sub>x</sub>Fe<sub>1-x</sub>Se<sub>2</sub> samples with other Ni:Fe ratios ( $x = 0.9$  and  $0.67$ ) was prepared by varying the Ni:Fe atomic ratio of the starting materials (see Methods for details). The formation of Ni<sub>x</sub>Fe<sub>1-x</sub>Se<sub>2</sub> was supported by X-ray photoelectron spectroscopy (XPS). In both Ni 2p<sub>3/2</sub> and Fe 2p<sub>3/2</sub> spectra (Fig. 2b and Supplementary Fig. 2), the main peaks have binding energies between those of the corresponding metal and metal oxides<sup>11,22,23</sup>. For example, the main peak at 853.5 eV in the Ni 2p<sub>3/2</sub> spectra has a binding energy between nickel metal (852.6 eV) and nickel oxides (853.7–854.9 eV). These binding energies are indicative of metal selenides. The Se 3d<sub>5/2</sub> binding energy of Ni<sub>x</sub>Fe<sub>1-x</sub>Se<sub>2</sub> is 55.2 eV, red-shifted from 55.4 eV for elemental Se (Fig. 2c)<sup>11</sup>. The minor broad peaks in Fig. 2b,c were attributed to surface impurities NiO<sub>x</sub>, FeO<sub>x</sub> and SeO<sub>2</sub>. This assignment is consistent with the previous finding that the surface of metal selenides is prone to oxidation by air<sup>11</sup>.

The morphology of as-prepared Ni<sub>x</sub>Fe<sub>1-x</sub>Se<sub>2</sub> ( $x = 0.8$ ) was first characterized by scanning electron microscopy (SEM). At the microscale, Ni<sub>x</sub>Fe<sub>1-x</sub>Se<sub>2</sub> inherited the morphology of NiFe LDH (Fig. 3a,b and Supplementary Fig. 3), and after selenization, nanoplates of ~150 nm in thickness were formed. Higher-magnification images, however, revealed that in contrast to NiFe LDH nanoplates which had a smooth surface (Supplementary Fig. 3b), Ni<sub>x</sub>Fe<sub>1-x</sub>Se<sub>2</sub> nanoplates were composed of numerous nanoparticles (Fig. 3b). The TEM image further revealed the porous hierarchical morphology of Ni<sub>x</sub>Fe<sub>1-x</sub>Se<sub>2</sub> (Fig. 3c). The nanoparticles were made of ultrathin nanosheets (Fig. 3d). HRTEM image indicated the single-crystal nature of each nanosheet (Fig. 3e). Lattice fringes were observed, with

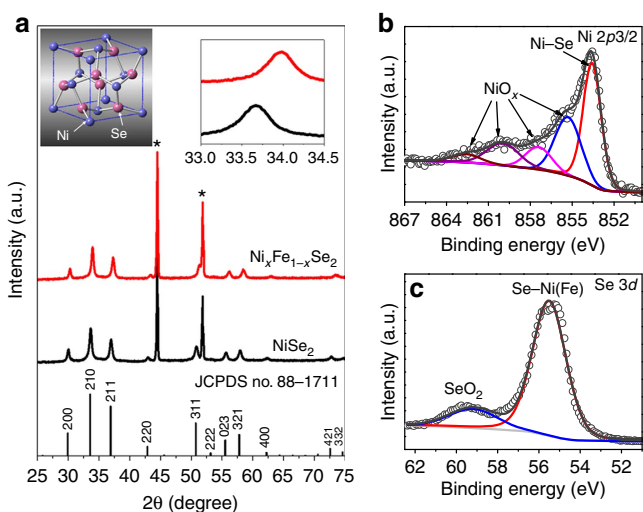


**Figure 2 | Characterization of Ni<sub>x</sub>Fe<sub>1-x</sub>Se<sub>2</sub>.** (a) PXRD patterns. The asterisks “\*” mark the diffraction peaks from the nickel foam substrate. The insets show the unit cell of cubic metal diselenides and the magnified PXRD patterns in the range between 33 and 34.5°. (b,c) High-resolution XPS of Ni 2p<sub>3/2</sub> (b) and Se 3d (c). The main peaks (red) are attributed to Ni<sub>x</sub>Fe<sub>1-x</sub>Se<sub>2</sub>, while the minor peaks are assigned to surface impurities of metal oxides and SeO<sub>2</sub>.

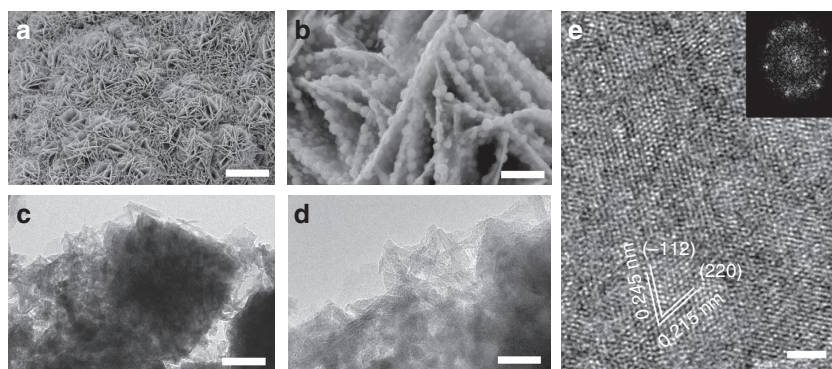


**Figure 3 | Structural characterization of Ni<sub>x</sub>Fe<sub>1-x</sub>Se<sub>2</sub>.** (a) SEM image of Ni<sub>x</sub>Fe<sub>1-x</sub>Se<sub>2</sub> nanoplates. (b) Magnified SEM image showing the nanoparticles grown on the nanoplates. (c) TEM image of a nanoparticle. (d) Magnified TEM image showing the nanosheets that make up the nanoplates. (e) HRTEM image of a nanosheet. The inset shows the FFT image of (e). Scale bars: (a) 10 μm; (b) 1 μm; (c) 50 nm; (d) 20 nm; and (e) 2 nm. FFT, fast-Fourier transform.

inter-planar distances of  $\sim 0.245$  and  $\sim 0.215$  nm, corresponding to the  $(-112)$  and  $(220)$  planes, respectively. The basal plane of the nanosheet is  $(111)$ , which was confirmed by fast-Fourier transform image (inset in Fig. 3e). Elemental mapping analysis (Supplementary Fig. 4) showed that Ni, Fe and Se were homogeneously distributed, consistent with the formation of single-phase  $\text{Ni}_x\text{Fe}_{1-x}\text{Se}_2$ . The atomic ratio of Se/Ni/Fe is  $\sim 7.3:2.6:1$ .

**In situ transformation.** As mentioned above, we expected that  $\text{Ni}_x\text{Fe}_{1-x}\text{Se}_2$  would be converted to  $\text{NiFeO}_x$  under OER conditions. This  $\text{Ni}_x\text{Fe}_{1-x}\text{Se}_2$ -derived oxide ( $\text{Ni}_x\text{Fe}_{1-x}\text{Se}_2$ -DO; we use 'DO' to designate the selenide-derived oxide from here on) was in fact our target catalyst. Our hope was that  $\text{Ni}_x\text{Fe}_{1-x}\text{Se}_2$ -DO would inherit the potentially beneficial nanostructure of  $\text{Ni}_x\text{Fe}_{1-x}\text{Se}_2$ . Thus,  $\text{Ni}_x\text{Fe}_{1-x}\text{Se}_2$ -DO was obtained by subjecting  $\text{Ni}_x\text{Fe}_{1-x}\text{Se}_2$  to

galvanostatic scan at the current density of  $5 \text{ mA cm}^{-2}$  until a stable potential was reached. SEM images (Fig. 4a,b) showed that  $\text{Ni}_x\text{Fe}_{1-x}\text{Se}_2$ -DO had a similar overall morphology to  $\text{Ni}_x\text{Fe}_{1-x}\text{Se}_2$ . TEM images (Fig. 4c,d) showed the nanosheets of  $\text{Ni}_x\text{Fe}_{1-x}\text{Se}_2$ -DO were only about 1–2 nm in thickness. HRTEM image (Fig. 4e) showed lattice fringes of  $\text{Ni}_x\text{Fe}_{1-x}\text{Se}_2$ -DO, which were different from those of  $\text{Ni}_x\text{Fe}_{1-x}\text{Se}_2$ . The inter-planar distance of  $0.261$  nm  $\text{Ni}_x\text{Fe}_{1-x}\text{Se}_2$ -DO was indexed to the  $(101)$  planes of metal hydroxides (for example, LDH or  $\alpha\text{-Ni}(\text{OH})_2$ ).

Elemental mapping was conducted to examine the change of composition after the *in situ* transformation. From  $\text{Ni}_x\text{Fe}_{1-x}\text{Se}_2$  to  $\text{Ni}_x\text{Fe}_{1-x}\text{Se}_2$ -DO, Ni and Fe remained homogeneously distributed, Se was removed, while oxygen was incorporated (Fig. 5a). Based on the energy-dispersive X-ray spectra (EDS), the Se content decreased from 67.1% in  $\text{Ni}_x\text{Fe}_{1-x}\text{Se}_2$  to 0.7% in  $\text{Ni}_x\text{Fe}_{1-x}\text{Se}_2$ -DO, and the oxygen content increased from undetectable in  $\text{Ni}_x\text{Fe}_{1-x}\text{Se}_2$  to 52.3% in  $\text{Ni}_x\text{Fe}_{1-x}\text{Se}_2$ -DO

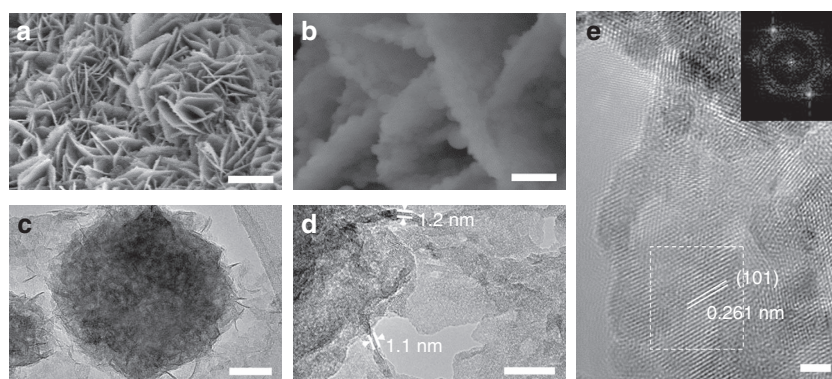


**Figure 4 | Structural characterization of  $\text{Ni}_x\text{Fe}_{1-x}\text{Se}_2$ -DO.** (a) SEM image of  $\text{Ni}_x\text{Fe}_{1-x}\text{Se}_2$ -DO nanoplates. (b) Magnified SEM image showing the nanoparticles grown on nanoplates. (c) TEM image of a nanoparticle. (d) Magnified TEM image showing the nanosheets that make up the nanoparticles. (e) HRTEM image of nanosheets. The inset shows the FFT image of the rectangle region in e. Scale bars: (a) 10  $\mu\text{m}$ ; (b) 1  $\mu\text{m}$ ; (c) 50 nm; (d) 10 nm; and (e) 2 nm. FFT, fast-Fourier transform

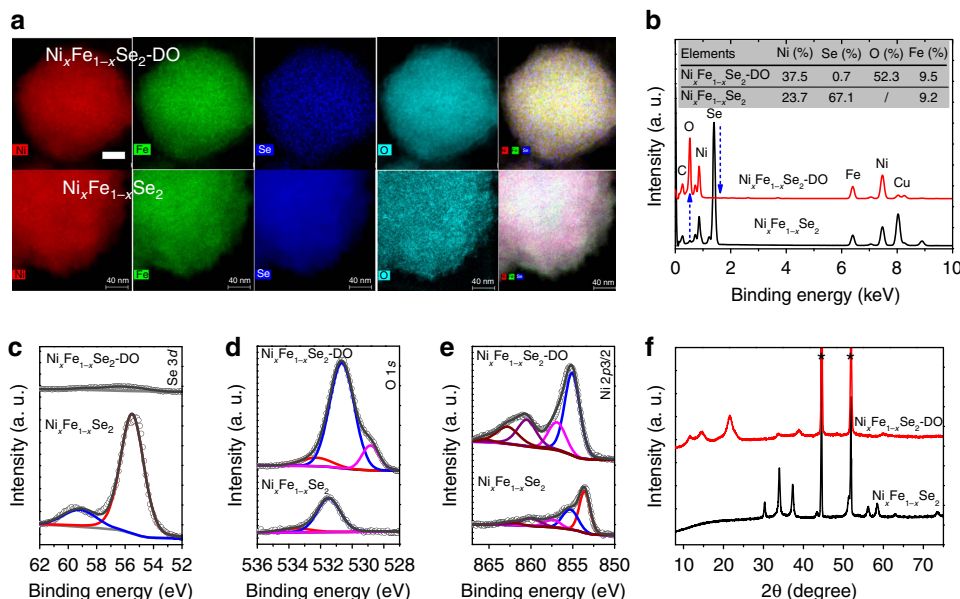
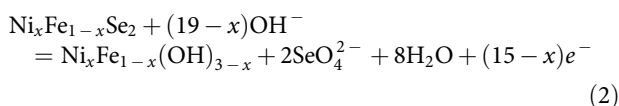
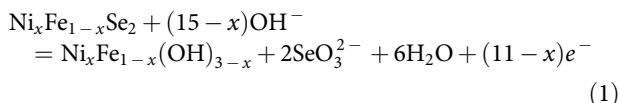


**Figure 5 | Comparison of  $\text{Ni}_x\text{Fe}_{1-x}\text{Se}_2$ -DO with  $\text{Ni}_x\text{Fe}_{1-x}\text{Se}_2$ .** (a,b) Elemental mapping images (a) and the corresponding EDS (b). Colour in elemental mapping images: red for Ni; green for Fe; blue for Se; cyan for O. Scar bar, 40 nm. The inset in the spectra shows the elemental atomic percentages. (c–e) High-resolution XPS spectra of Se 3d (c) O 1s (d) and Ni 2p<sub>3/2</sub> (e). In O1s, the minor peaks of 528.8 and 532.3 eV can be assigned to lattice oxygen ( $\text{O}^{2-}$ ) and adsorbed molecular water, respectively. (f) PXRD patterns. The asterisks '\*' mark the diffraction peaks from the nickel foam substrate. EDS, energy-dispersive spectroscopy.

(Fig. 5b). The compositional change was further confirmed by high-resolution XPS spectra (Fig. 5c–e). The Se 3d peak nearly vanished while the O 1s peak increased dramatically in intensity. The main peak in the O 1s spectrum was at 530.6 eV, attributed to Ni-OH or Fe-OH (ref. 24). On the basis of the XPS spectra, the atomic percentages of O and Se were  $\sim 47.7\%$  and  $1.29\%$  in  $\text{Ni}_x\text{Fe}_{1-x}\text{Se}_2\text{-DO}$ , in agreement with the EDS results. The Ni 2p<sub>3/2</sub> peak was shifted from 853.5 eV in  $\text{Ni}_x\text{Fe}_{1-x}\text{Se}_2$  to 855.1 eV in  $\text{Ni}_x\text{Fe}_{1-x}\text{Se}_2\text{-DO}$ , also consistent with the formation of  $\text{NiFeO}_x$ . Finally, the PXRD pattern of  $\text{Ni}_x\text{Fe}_{1-x}\text{Se}_2\text{-DO}$  (Fig. 5f) also indicated the disappearance of  $\text{Ni}_x\text{Fe}_{1-x}\text{Se}_2$  and the formation of a crystalline  $\text{NiFeO}_x$  phase. Based on previous studies of the electrochemical oxidation of NiSe and MoSe<sub>2</sub> in basic solutions<sup>25</sup>, the *in situ* transformation is proposed to occur via the following pathways:



**Oxygen-evolution catalysis.** The electrocatalytic activity of  $\text{Ni}_x\text{Fe}_{1-x}\text{Se}_2\text{-DO}$ , NiFe LDH, NiSe<sub>2</sub>-DO, NiSe-DO and Ni foam (NF) towards OER in 1 M KOH oxidation was measured and compared (see Methods for details). As shown in Fig. 6a,  $\text{Ni}_x\text{Fe}_{1-x}\text{Se}_2\text{-DO}$  is the best catalyst among the five compounds, giving much higher current density (*J*) at the same overpotential ( $\eta$ ). To reach  $J = 10 \text{ mA cm}^{-2}$ ,  $\text{Ni}_x\text{Fe}_{1-x}\text{Se}_2\text{-DO}$  required an overpotential of only 195 mV, which was 49, 46, 58 and 96 mV less than that of NiFe LDH, NiSe<sub>2</sub>-DO, NiSe-DO and NF, respectively (Fig. 6b). The current density at  $\eta = 250 \text{ mV}$  was  $262 \text{ mA cm}^{-2}$ , which was 16-, 18-, 29- and 262-fold higher than those of NiFe LDH, NiSe<sub>2</sub>-DO, NiSe-DO and NF, respectively (Fig. 6c). In fact, the activity of  $\text{Ni}_x\text{Fe}_{1-x}\text{Se}_2\text{-DO}$  is superior to other state-of-the-art catalysts (Supplementary Table 1). NiFe LDH has been regarded as the most active OER catalyst in alkaline conditions. Lu *et al.*<sup>26</sup> reported the overpotential of  $\sim 256 \text{ mV}$  for  $10 \text{ mA cm}^{-2}$  by NiFe LDH grown on Ni foam. The catalytic activity of NiFe LDH was further improved by applying an improved electrosynthesis method<sup>27</sup>. However, an overpotential of 224 mV for  $10 \text{ mA cm}^{-2}$  was still required. The activity of  $\text{Ni}_x\text{Fe}_{1-x}\text{Se}_2\text{-DO}$  compares favourably even to the best hybrid catalysts made of  $\text{NiFeO}_x$  and carbon nanomaterials. Ma *et al.*<sup>28</sup> reported that the NiFe hydroxide/graphene superlattice reached  $10 \text{ mA cm}^{-2}$  at an overpotential of 210 mV. Hou *et al.*<sup>29</sup> reported that exfoliated graphene/Co<sub>0.85</sub>Se/NiFe LDH composites catalysed OER with an overpotential of 203 mV for  $10 \text{ mA cm}^{-2}$ . The most active hybrid catalyst, r-GO/NiFe LDH, was reported by Long *et al.*,<sup>30</sup> which gave  $10 \text{ mA cm}^{-2}$  at an overpotential of 195 mV. It was proposed that the activity of these hybrid materials originated from a synergetic effect between  $\text{NiFeO}_x$  and carbon nanomaterials (CNT, r-GO and carbon quantum dots). Thus, our  $\text{Ni}_x\text{Fe}_{1-x}\text{Se}_2\text{-DO}$  is until now the most active single-phase catalyst, and even higher activity might be achieved by coupling it to carbon nanomaterials. The influence of Ni:Fe atomic ratio on the OER activity was probed. The highest activity was obtained at  $x = 0.8$ , while the samples with  $x = 0.9$  and 0.67 exhibited only modestly lower activity (Supplementary Fig. 5). This result is consistent with previous reports that the activity of  $\text{NiFeO}_x$  varied only slightly when the Fe:Ni ratio was changed from 0.1 and 0.55 (refs 18,31).

By plotting overpotential against  $\log(J)$ , the kinetic parameters of OER by the five catalysts were calculated (Fig. 6d). The  $\text{Ni}_x\text{Fe}_{1-x}\text{Se}_2\text{-DO}$  has a Tafel slope of about  $28 \text{ mV dec}^{-1}$ , close to that of NiFe LDH ( $32 \text{ mV dec}^{-1}$ ), but much smaller than the other catalysts ( $40\text{--}54 \text{ mV dec}^{-1}$ ). We further compared the electrochemical surface area (ECSA), estimated from their double-layer capacitance ( $C_{dl}$ ) of  $\text{Ni}_x\text{Fe}_{1-x}\text{Se}_2\text{-DO}$  and NiFe LDH. The ECSA of  $\text{Ni}_x\text{Fe}_{1-x}\text{Se}_2\text{-DO}$  is 2.4-fold of the ECSA of NiFe LDH (Fig. 6e) that does not account for the 16-fold higher catalytic activity of the former. We attribute the superior activity of  $\text{Ni}_x\text{Fe}_{1-x}\text{Se}_2\text{-DO}$  to its desirable nanostructure. As shown in Fig. 4,  $\text{Ni}_x\text{Fe}_{1-x}\text{Se}_2\text{-DO}$  nanoparticles are made of ultrathin nanosheets. If the edges of  $\text{NiFeO}_x$  are the active sites, then a higher number of active sites is expected on  $\text{Ni}_x\text{Fe}_{1-x}\text{Se}_2\text{-DO}$  than other forms of  $\text{NiFeO}_x$ . To provide additional support for this hypothesis, the microstructures of  $\text{Ni}_x\text{Fe}_{1-x}\text{Se}_2\text{-DO}$  was compared with NiFe LDH, one of the most active forms of  $\text{NiFeO}_x$  (refs 26,27). SEM images show that NiFe LDH is made of large single-crystalline nanoplates whereas  $\text{Ni}_x\text{Fe}_{1-x}\text{Se}_2\text{-DO}$  is made of highly porous nanoplates consisting of ultrathin nanosheets (Supplementary Fig. 6). Thus,  $\text{Ni}_x\text{Fe}_{1-x}\text{Se}_2\text{-DO}$ 's particle size is much smaller than NiFe LDH. The porosity of  $\text{Ni}_x\text{Fe}_{1-x}\text{Se}_2\text{-DO}$  and NiFe LDH were probed by N<sub>2</sub> adsorption–desorption measurements. Compared with NiFe LDH, more pores were formed in  $\text{Ni}_x\text{Fe}_{1-x}\text{Se}_2\text{-DO}$  (Supplementary Fig. 7). More importantly, an additional sharp peak was observed at a size range of 2.5–4 nm for  $\text{Ni}_x\text{Fe}_{1-x}\text{Se}_2\text{-DO}$ , indicating the formation of tiny nanopores. The nanoporosity resulted in a high Brunauer-Emmett-Teller (BET) surface area of  $109 \text{ m}^2 \text{ g}^{-1}$  for  $\text{Ni}_x\text{Fe}_{1-x}\text{Se}_2\text{-DO}$ , which is 8.3 times higher than that of NiFe LDH. The higher porosity and smaller particle size of  $\text{Ni}_x\text{Fe}_{1-x}\text{Se}_2\text{-DO}$  compared with NiFe LDH would lead to higher number of edge sites in the former, which might explain its superior catalytic activity. The molecular origin of this activity is subject to further studies.

The stability of OER catalysed by the  $\text{Ni}_x\text{Fe}_{1-x}\text{Se}_2\text{-DO}$  electrode was tested at a constant current density *J* of  $10 \text{ mA cm}^{-2}$  for 24 h. Figure 6f shows that after an activation period of 0.5 h, the overpotential remained at  $\sim 195 \text{ mV}$  during 24 h. The Faradaic efficiency of OER was determined using a fluorescence O<sub>2</sub> probe. A quantitative yield was found quantitative during a 6.5 h electrolysis experiment (inset in Fig. 6f).

## Discussion

In summary, using NiSe as a representative example of metal selenides, we show that metal selenides are converted into metal oxides or hydroxides under OER conditions. These oxides or hydroxides are responsible for the catalytic activity of metal selenides in OER. Taking advantage of this *in situ* transformation, we prepared for the first time a nickel iron diselenide ( $\text{Ni}_x\text{Fe}_{1-x}\text{Se}_2$ ) and used it as a templating precursor to ultrathin nanosheets of the corresponding oxide,  $\text{Ni}_x\text{Fe}_{1-x}\text{Se}_2\text{-DO}$ . A current density of  $10 \text{ mA cm}^{-2}$  is obtained at an overpotential of only 195 mV in alkaline solutions using  $\text{Ni}_x\text{Fe}_{1-x}\text{Se}_2\text{-DO}$  as the catalyst, making it one of the most active OER catalyst reported to date. The templating approach described here might be applicable for the synthesis of other metal oxide-based nanomaterials.

## Methods

**Materials synthesis.** Both NiSe<sub>2</sub> and  $\text{Ni}_x\text{Fe}_{1-x}\text{Se}_2$  were prepared through two steps: (i) metal hydroxide precursors were grown on nickel foam via a hydrothermal method; and (ii) hydroxide precursors were converted into diselenides via a solvothermal selenization treatment. 'x' represents the Ni ratio in the total metal elements of the starting solution. Typically, for  $\text{Ni}_x\text{Fe}_{1-x}\text{Se}_2$  ( $x = 0.8$ ),  $\text{Ni}(\text{NO}_3)_2 \cdot 6\text{H}_2\text{O}$  (2.0 mmol, 582 mg),  $\text{FeSO}_4 \cdot 7\text{H}_2\text{O}$  (0.5 mmol, 139 mg),  $\text{NH}_4\text{F}$  (10 mmol, 370 mg) and urea (25 mmol, 1,501 mg) were dissolved in H<sub>2</sub>O (40 ml). The as-obtained solution together with one piece of nickel foam ( $5 \times 30 \text{ mm}$ ) were then sealed in a 45 ml Teflon-lined stainless steel autoclave and heated at  $120^\circ \text{C}$  in

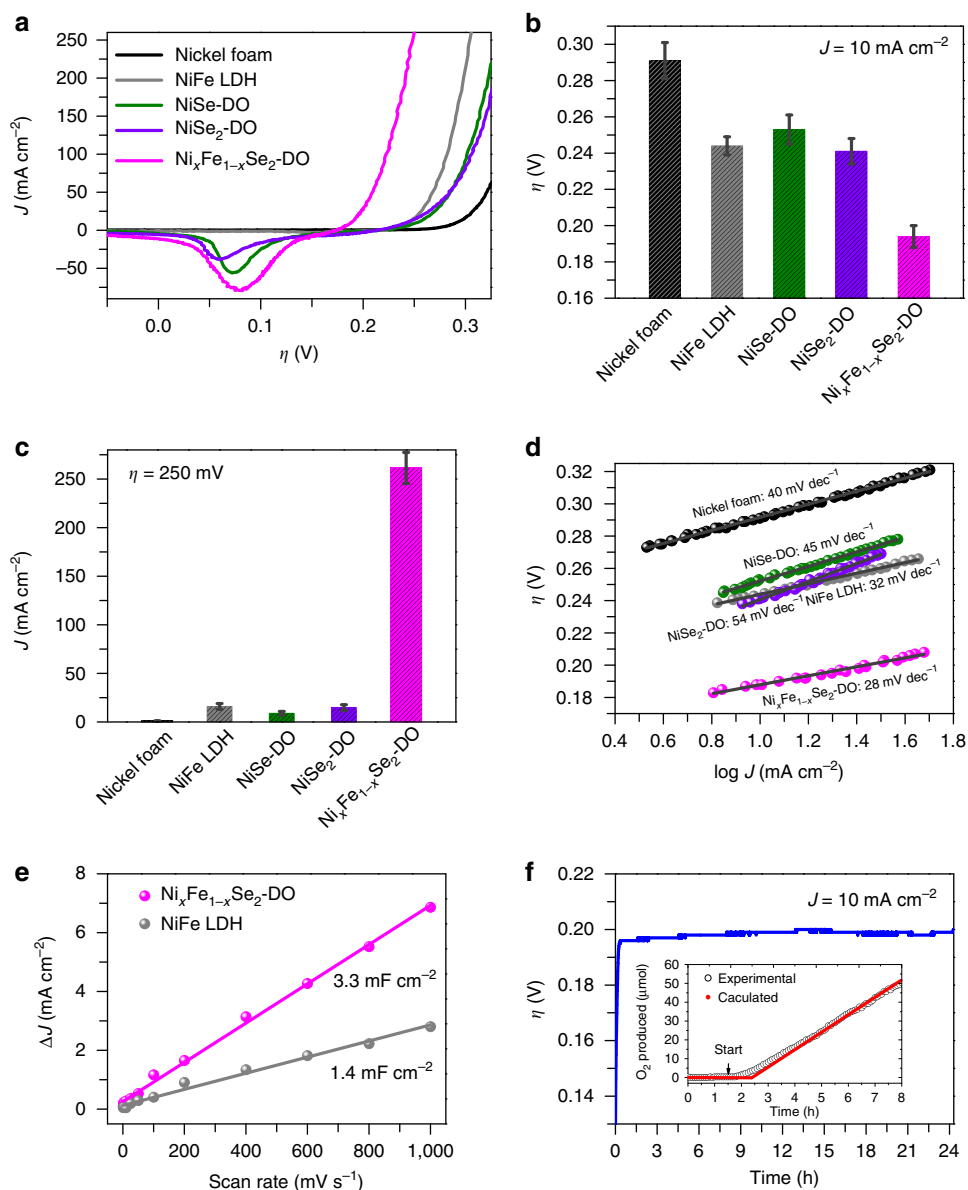


**Figure 6 | Electrochemical characterization.** (a) Polarization curves; (b) overpotential required for  $J = 10 \text{ mA cm}^{-2}$ ; (c) current densities at  $\eta = 250 \text{ mV}$ ; and (d) Tafel plots for  $\text{Ni}_x\text{Fe}_{1-x}\text{Se}_2\text{-DO}$ , NiFe LDH, NiSe<sub>2</sub>-DO, NiSe-DO and NF. The error bar represents the range of results from three independent measurements. (e) Capacitive  $J$  versus scan rate for  $\text{Ni}_x\text{Fe}_{1-x}\text{Se}_2\text{-DO}$  and NiFe LDH. The linear slope is equivalent to twice of the double-layer capacitance  $C_{dl}$ . (f) Chronopotentiometric measurements of OER at  $10 \text{ mA cm}^{-2}$  using  $\text{Ni}_x\text{Fe}_{1-x}\text{Se}_2\text{-DO}$  as catalyst. The inset shows the calculated versus actual oxygen production catalyzed by a constant current of  $1 \text{ mA}$ . The calculated value represent the expected amount of  $\text{O}_2$  assuming a quantitative Faradaic yield for  $\text{O}_2$  formation.

an electric oven for 16 h. After being washed thoroughly with distilled water and absolute ethanol, the as-prepared nickel foam coated with NiFe hydroxides was submerged into another 45 ml autoclave containing Se (3.75 mmol, 296 mg), NaOH (7.5 mmol, 300 mg), hydrazine (0.14 ml) and dimethylformamide (DMF) (25 ml). After keeping at  $180^\circ\text{C}$  for 1 h,  $\text{Ni}_x\text{Fe}_{1-x}\text{Se}_2$  was obtained. To synthesize  $\text{Ni}_x\text{Fe}_{1-x}\text{Se}_2$  ( $x = 1, 0.9$  and  $0.67$ ) with variable Ni:Fe ratios,  $\text{Ni}(\text{NO}_3)_2 \cdot 6\text{H}_2\text{O}$  and  $\text{FeSO}_4 \cdot 7\text{H}_2\text{O}$  with the desired molar ratio were dissolved in water with a total quantity of 2.5 mmol. When  $x = 1$ , NiSe<sub>2</sub> was obtained.

**Materials characterization.** PXRD patterns were recorded on an X'Pert Philips diffractometer with monochromatic  $\text{Cu}_{K\alpha}$  radiation ( $\lambda = 1.540598 \text{ \AA}$ ) and a fast Si-PIN multi-strip detector. As-synthesized NiSe<sub>2</sub> and  $\text{Ni}_x\text{Fe}_{1-x}\text{Se}_2$  were used directly for PXRD measurements. Morphology and microstructure was examined by a Phillips (FEI) XLF-30 FEG SEM and a FEI Tecnai Osiris TEM equipped with high-brightness field emission gun (XFEG). Energy-dispersive X-ray spectroscopy (EDX) mapping images were taken under a scanning TEM modal. Samples for TEM were prepared by drop-drying the samples from their diluted ethanol

suspensions onto carbon-coated copper grids. XPS measurements were performed on a PHI5000 VersaProbe II XPS system by Physical Electronics (PHI) with a detection limit of one atomic per cent. Monochromatic X-rays were generated by an Al  $K\alpha$  source (14,867 eV). The diameter of the analysed area is  $10 \mu\text{m}$ .  $\text{N}_2$  adsorption-desorption measurements were conducted on Micromeritics 3Flex adsorption analyser at 77K. Before the measurements, the samples were degassed at  $100^\circ\text{C}$  under vacuum for 1 h. Pore size distributions were calculated by the Barrett-Joyner-Halenda (BJH) method from the desorption branches of the isotherms.

**Electrochemical measurement.** Electrochemical characterizations including cyclic voltammetry (CV), LSV and chronopotentiometry were carried out on a Gamry Reference 3000 electrochemical instrument using a three-electrode electrochemical system. A 1 M KOH solution was used as electrolyte, and an Ag/AgCl electrode with saturated KCl filling solution and Pt wire were used as reference and counter electrodes, respectively. For catalyst grown on nickel foam (NiSe<sub>2</sub>,  $\text{Ni}_x\text{Fe}_{1-x}\text{Se}_2$  and NiFe-LDH), they were used as work electrodes directly. Hot glue was employed to fix the working area at  $0.2 \text{ cm}^{-2}$  ( $0.5 \times 0.4 \text{ cm}$ ).

Before test, the reference electrode was measured against another unused Ag/AgCl reference electrode stored in saturated KCl solution. Calibration of Ag/AgCl reference electrodes was done by measuring the reversible hydrogen electrode (RHE) potential using a Pt electrode under a H<sub>2</sub> atmosphere. During the test, Ag/AgCl reference electrode was constructed to a double-junction electrode to minimize contact between KOH and KCl. CVs were performed at a scan rate of 1 mV s<sup>-1</sup>, and the average of the two potentials at which the current crossed zero was taken to be the thermodynamic potential for the hydrogen electrode reaction. In 1 M KOH electrolytes,  $E_{vs,RHE} = E_{vs,Ag/AgCl} + 1.009$  V, and overpotential for OER was  $\eta = E_{vs,RHE} - 1.23$  V =  $E_{vs,Ag/AgCl} - 0.221$  V. Ohmic drop correction was performed using the current interrupt method by the potentiostat. Before recording the catalytic activity, catalysts were activated by a chronopotentiometry scan with constant current density of 5–10 mA cm<sup>-2</sup> until reaching a stable state. Normally, we set the pretreatment time at 12 h. Following the preconditioning, two cycles of LSVs were measured at a scan rate of 1 mV s<sup>-1</sup>. Tafel slopes were calculated based on the LSV curves by plotting overpotential against log(current density). Chronopotentiometry measurements were performed to evaluate the long-term stability. The ECSA was determined by measuring the capacitive current associated with double-layer charging from the scan-rate dependence of CVs. For this, the potential window of CVs was 0.2–0.3 V versus Ag/AgCl. The scan rates were 5, 10, 25, 50, 100, 200, 400, 600, 800 and 1,000 mV s<sup>-1</sup>. The double-layer capacitance ( $C_{dl}$ ) was estimated by plotting the  $\Delta J = (J_a - J_c)$  at 0.25 V versus Ag/AgCl against the scan rate. The linear slope is twice of the double-layer capacitance  $C_{dl}$ . The measurements of O<sub>2</sub> were performed using an Ocean Optics Multifrequency Phase Fluorimeter (MFPF-100) with a FOXY-OR 125 probe (see in Supplementary Methods).

**Data availability.** The data that support the findings of this study are available from the corresponding authors upon request.

## References

- Lewis, N. S. & Nocera, D. G. Powering the planet: chemical challenges in solar energy utilization. *Proc. Natl Acad. Sci. USA* **103**, 15729–15735 (2006).
- Dau, H. *et al.* The mechanism of water oxidation: from electrolysis via homogeneous to biological catalysis. *ChemCatChem* **2**, 724–761 (2010).
- Singh, A. & Spiccia, L. Water oxidation catalysts based on abundant first row transition metals. *Coord. Chem. Rev.* **257**, 2607–2622 (2013).
- Galan-Mascaros, J. R. Water oxidation at electrodes modified with earth-abundant transition-metal catalysts. *ChemElectroChem* **2**, 37–50 (2015).
- Stern, L. A., Feng, L. G., Song, F. & Hu, X. L. Ni<sub>2</sub>P as a Janus catalyst for water splitting: the oxygen evolution activity of Ni<sub>2</sub>P nanoparticles. *Energy Environ. Sci.* **8**, 2347–2351 (2015).
- Ryu, J., Jung, N., Jang, J. H., Kim, H. J. & Yoo, S. J. *In situ* transformation of hydrogen-evolving CoP nanoparticles: toward efficient oxygen evolution catalysts bearing dispersed morphologies with Co-oxo/hydroxo molecular units. *ACS Catal.* **5**, 4066–4074 (2015).
- Wang, P., Song, F., Amal, R., Ng, Y. H. & Hu, X. Efficient water splitting catalyzed by cobalt phosphide-based nanoneedle arrays supported on carbon cloth. *ChemSusChem* **9**, 472–477 (2016).
- Chen, W. *et al.* *In situ* electrochemical oxidation tuning of transition metal disulfides to oxides for enhanced water oxidation. *ACS Central Sci.* **1**, 244–251 (2015).
- Tang, C., Cheng, N., Pu, Z., Xing, W. & Sun, X. NiSe nanowire film supported on nickel foam: an efficient and stable 3D bifunctional electrode for full water splitting. *Angew. Chem. Int. Ed. Engl.* **54**, 9351–9355 (2015).
- Swesi, A. T., Masud, J. & Nath, M. Nickel selenide as a high-efficiency catalyst for oxygen evolution reaction. *Energy Environ. Sci.* **9**, 1771–1782 (2016).
- Kwak, I. H. *et al.* CoSe<sub>2</sub> and NiSe<sub>2</sub> nanocrystals as superior bifunctional catalysts for electrochemical and photoelectrochemical water splitting. *ACS Appl. Mater. Interfaces* **8**, 5327–5334 (2016).
- Yang, J. *et al.* Shape control and characterization of transition metal diselenides MSe<sub>2</sub> (M = Ni, Co, Fe) prepared by a solvothermal-reduction process. *Chem. Mater.* **13**, 848–853 (2001).
- Zhuang, Z., Peng, Q., Zhuang, J., Wang, X. & Li, Y. Controlled hydrothermal synthesis and structural characterization of a nickel selenide series. *Chem. A Eur. J.* **12**, 211–217 (2006).
- Yuan, B. X., Luan, W. L. & Tu, S. T. One-step solvothermal synthesis of nickel selenide series: composition and morphology control. *CrystEngComm* **14**, 2145–2151 (2012).
- Yuan, B. X., Luan, W. L. & Tu, S. T. One-step synthesis of cubic FeS<sub>2</sub> and flower-like FeSe<sub>2</sub> particles by a solvothermal reduction process. *Dalton Trans.* **41**, 772–776 (2012).
- Stern, L. A. & Hu, X. L. Enhanced oxygen evolution activity by NiO<sub>x</sub> and Ni(OH)<sub>2</sub> nanoparticles. *Faraday Discuss.* **176**, 363–379 (2014).
- Gao, M. *et al.* Efficient water oxidation using nanostructured  $\alpha$ -nickel-hydroxide as an electrocatalyst. *J. Am. Chem. Soc.* **136**, 7077–7084 (2014).
- Trotochaud, L., Young, S. L., Ranney, J. K. & Boettcher, S. W. Nickel-iron oxyhydroxide oxygen-evolution electrocatalysts: the role of intentional and incidental iron incorporation. *J. Am. Chem. Soc.* **136**, 6744–6753 (2014).
- Friebel, D. *et al.* Identification of highly active Fe sites in (Ni,Fe)OOH for electrocatalytic water splitting. *J. Am. Chem. Soc.* **137**, 1305–1313 (2015).
- Smith, R. D. L. *et al.* Photochemical route for accessing amorphous metal oxide materials for water oxidation catalysis. *Science* **340**, 60–63 (2013).
- Morales-Guio, C. G. *et al.* An optically transparent iron nickel oxide catalyst for solar water splitting. *J. Am. Chem. Soc.* **137**, 9927–9936 (2015).
- Grosvenor, A. P., Biesinger, M. C., Smart, R. S. & McIntyre, N. S. New interpretations of XPS spectra of nickel metal and oxides. *Surf. Sci.* **600**, 1771–1779 (2006).
- Biesinger, M. C. *et al.* Resolving surface chemical states in XPS analysis of first row transition metals, oxides and hydroxides: Cr, Mn, Fe, Co and Ni. *Appl. Surf. Sci.* **257**, 2717–2730 (2011).
- Ali-Loytty, H. *et al.* Ambient-pressure XPS study of a Ni-Fe electrocatalyst for the oxygen evolution reaction. *J. Phys. Chem. C* **120**, 2247–2253 (2016).
- Franklin, T. C., Adeniyi, W. K. & Nnodimele, R. The electrooxidation of some insoluble inorganic sulfides, selenides, and tellurides in cationic surfactant-aqueous sodium-hydroxide systems. *J. Electrochem. Soc.* **137**, 480–484 (1990).
- Lu, Z. *et al.* Three-dimensional NiFe layered double hydroxide film for high-efficiency oxygen evolution reaction. *Chem. Commun.* **50**, 6479–6482 (2014).
- Li, Z. H. *et al.* Fast electrosynthesis of Fe-containing layered double hydroxide arrays toward highly efficient electrocatalytic oxidation reactions. *Chem. Sci* **6**, 6624–6631 (2015).
- Ma, W. *et al.* A superlattice of alternately stacked Ni-Fe hydroxide nanosheets and graphene for efficient splitting of water. *ACS Nano* **9**, 1977–1984 (2015).
- Hou, Y. *et al.* Vertically oriented cobalt selenide/NiFe layered-double-hydroxide nanosheets supported on exfoliated graphene foil: an efficient 3D electrode for overall water splitting. *Energy Environ. Sci.* **9**, 478–483 (2016).
- Long, X. *et al.* A strongly coupled graphene and FeNi double hydroxide hybrid as an excellent electrocatalyst for the oxygen evolution reaction. *Angew. Chem. Int. Ed. Engl.* **53**, 7584–7588 (2014).
- Louie, M. W. & Bell, A. T. An investigation of thin-film Ni-Fe oxide catalysts for the electrochemical evolution of oxygen. *J. Am. Chem. Soc.* **135**, 12329–12337 (2013).

## Acknowledgements

This work is supported by the EPFL and the Swiss Government Excellence Postdoc Fellowship. We thank Dr. Kurt Schenk for help with PXRD, the Interdisciplinary Center for Electron Microscopy at EPFL assistance in electron microscopic measurements and XPS, and Florent Héroguel and Prof. Jeremy Luterbacher (EPFL) for the N<sub>2</sub> adsorption-desorption measurement.

## Author contributions

F.S. and X.H. conceived and directed the project. X.X. and F.S. fabricated the materials, did the structural characterization and tested the electrochemical activity. All authors analysed the data. F.S. and X.H. wrote the paper, with input from X.X.

## Additional information

**Supplementary Information** accompanies this paper at <http://www.nature.com/naturecommunications>

**Competing financial interests:** A priority patent application on the synthesis and application of NiFeSe<sub>2</sub> has been filed by EPFL; EP Patent Application Nr 16180605.4, 'New catalysts for oxygen evolution reaction'. The inventors of the patent application are authors F.S. and X.H. The remaining author declares no competing financial interests.

**Reprints and permission** information is available online at <http://ngp.nature.com/reprintsandpermissions/>

**How to cite this article:** Xu, X. *et al.* A nickel iron diselenide derived efficient oxygen evolution catalyst. *Nat. Commun.* **7**:12324 doi: 10.1038/ncomms12324 (2016).



This work is licensed under a Creative Commons Attribution 4.0 International License. The images or other third party material in this article are included in the article's Creative Commons license, unless indicated otherwise in the credit line; if the material is not included under the Creative Commons license, users will need to obtain permission from the license holder to reproduce the material. To view a copy of this license, visit <http://creativecommons.org/licenses/by/4.0/>

© The Author(s) 2016